Optimum Design and Comparison of Slip Permanent-Magnet Couplings With Wind Energy as Case Study Application

Johannes H. J. Potgieter, *Student Member, IEEE*, and Maarten J. Kamper, *Senior Member, IEEE*

***Abstract*—With eddy-current couplings proposed for and applied in several industrial applications, it is essential that these types of electrical machines be more thoroughly evaluated. In this paper, the feasibility of replacing the classical eddy-current coupling topology with a toothed slip permanent magnet coupling (PMC) is investigated. The case study application in this paper for the slip PMC is for a new type of wind generator concept known as a slip synchronous permanent magnet generator. Several different slip PMC technologies are evaluated, and a number of interesting novel concepts are introduced. These different topologies are optimized by means of finite element (FE) analysis for minimum active mass. The FE results are verified with practical measurements on several different prototypes.**

***Index Terms*—Design optimization, eddy-current coupling, permanent-magnet (PM) machines, slip permanent-magnet coupling (PMC), torque converters, wind energy.**

I. Nomenclature

B_{demag}	Minimum demagnetization permanent-magnet (PM) flux density, in teslas.
D_i	Inside diameter of slip permanent-magnet coupling (PMC), in millimeters.
D_o	Outside diameter of slip PMC, in millimeters.
E_r	Induced slip-rotor bar voltage, in volts.
f_r	Torque ripple frequency of slip PMC, in hertzs.
f_s	Grid frequency, in hertzs.
h_m	Magnet height, in millimeters.
I_d	d-axis current of slip rotor, in amperes.
I_q	q-axis current of slip rotor, in amperes.
I_r	RMS current of slip rotor, in amperes.
K_r	Machine constant used for brushless dc modeling.
l	Active length of slip PMC, in millimeters.
L_d	d-axis inductance of slip rotor, in henries.
L_q	q-axis inductance of slip rotor, in henries.
L_e	End-winding inductance of slip rotor, in henries.
L_r	Bar inductance, in henries.
m	Amount of active slip-rotor slots.
M_{Cond}	Conductor mass, in kilograms.
M_{Fe}	Steel mass, in kilograms.
M_{PM}	PM mass, in kilograms.
M_{Tot}	Total active mass, in kilograms.
n	Harmonic order.
p	Number of slip-PMC poles.
P_{cu}	Conductor loss in slip rotor, in watts.
P_r	Output power of slip PMC, in kilowatts.
P_s	Electrical output power of the slip synchronous permanent magnet generator (SS PMG), in kilowatts.
P_t	Mechanical turbine input power, in kilowatts.
R_r	Bar resistance of slip rotor, in ohms.
S	Amount of slip-rotor slots.
s	Per-unit slip, in per unit (p.u.)
T_b	Breakdown torque of slip PMC, in newton meters.
T_r	Steady-state torque of slip PMC, in newton meters.
T_s	Steady-state PM synchronous generator (PMSG) stator torque, in newton meters.
t	Time, in seconds.
t_{sl}	Electrical period of slip PMC, in seconds.
v_w	Wind speed, in meters per second.
w_{off}	Dead-time region of slip-rotor bar current, in seconds.
w_{on}	Conducting region of slip-rotor bar current, in seconds.
α_r	Current angle, in degrees.
$\Delta\tau_{\mathrm{L}}$	Load torque ripple, in percent.
$\Delta\tau_{\mathrm{NL}}$	No-load cogging torque, in percent.
$\Delta\tau_s$	PMSG stator torque response disturbance, in per unit.
η_r	Efficiency of slip PMC, in percent.
λ_d	d-axis flux linkage, in weber turns.
λ_q	q-axis flux linkage, in weber turns.
λ_m	PM flux linkage, in weber turns.
λ_r	Per bar flux linkage of slip PMC, in weber turns.
σ_m	Magnet pitch to pole pitch ratio, in per unit.
ω_b	Speed point corresponding to T_b, in radians per second.
ω_s	Electrical PM rotor speed, in radians per second.
ω_{sl}	Electrical slip speed, in radians per second.
ω_t	Electrical turbine speed, in radians per second.

The subscript m denotes mechanical quantity, and the subscript bar refers to the parameters of the slip PMC per bar.

Manuscript received October 8, 2013; revised December 12, 2013; accepted January 24, 2014. Date of publication February 12, 2014; date of current version September 16, 2014. Paper 2013-EMC-632.R1, presented at the 2012 IEEE Energy Conversion Congress and Exposition, Raleigh, NC, USA, September 15–20, and approved for publication in the IEEE Transactions on Industry Applications by the Electric Machines Committee of the IEEE Industry Applications Society.

The authors are with the Department of Electrical and Electronic Engineering, Stellenbosch University, Stellenbosch 7600, South Africa (e-mail: jpot101@gmail.com; kamper@sun.ac.za).

Color versions of one or more of the figures in this paper are available online at http://ieeexplore.ieee.org.

Digital Object Identifier 10.1109/TIA.2014.2305796

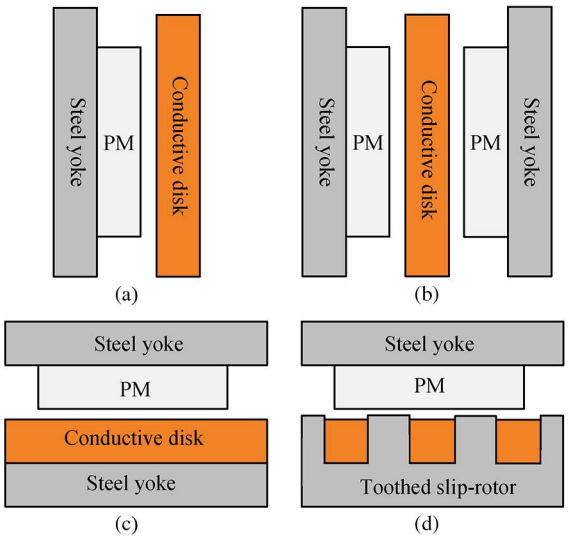

Fig. 1. Different eddy-current coupling configurations. (a) Single-sided configuration with only a field member and a conductive structure. (b) Double-sided topology. (c) Single-sided topology with a yoke provided for the conductive structure. (d) Toothed slip PMC.

II. Introduction

Eddy-current couplings are employed in many industrial applications for power transmission [1]–[7]. Some of the advantages of eddy-current couplings due to there being no mechanical or frictional contact are faster response times, increased damping of torque transients, better susceptibility to misalignment, much more isolation between loads during overtorque conditions, reduced wear, reduced maintenance, and increased reliability and lifetime of components. The eddy-current coupling consists of a field member, comprising of either electromagnets, as was commonly used in the past, or PMs, which are more frequently used in newer applications, and a conductive disk or ring, in which eddy-currents are induced. These couplings operate on the principle of slip, where more eddy-currents are induced with an increase in speed, which means that more power is dissipated in the conductive part of the coupling. Typical eddy-current coupling topologies from literature are shown in Fig. 1(a)–(d). The simplest topology, as shown in Fig. 1(a), consists of a field member and a conductive disk or ring. In Fig. 1(b), a double-rotor topology is employed, and in Fig. 1(c), a back yoke is added to the conductive structure in order to improve the flux linking through the conducting part of the coupling. Both radial and axial flux eddy-current couplings are used, with axial flux topologies used in many cases, due to their ability to adjust the air gap for some margin of torque control. This, however, increases the mechanical complexity of the device. It is possible to obtain torque control by adjusting the field strength if electromagnets are used, but these types of couplings are not as popular anymore due to their high mass and large size. In [5], it is mentioned for PM topologies that, if the conducting structure is wound, it is possible to add an external resistance to the winding to achieve some margin of torque control. Again, however, the added complexity of the windings and external resistance circuit may present problems.

In general, the application of eddy-current couplings is limited by their cost and mass. It is thus clear that significant scope exists to reduce the mass and the cost of these systems. Utilizing a topology as shown in Fig. 1(d), with a toothed layout similar to conventional electrical machines, is mentioned in [5] but not investigated further. The working principle of such a coupling, referred to in this paper as a slip PMC, is basically the same as that of a short-circuited PM machine and can be thus modeled as such. It is true that, by using this type of layout, the complexity of the device might increase, but due to the effective air gap being reduced, it is evident that large potential exists to reduce the PM content, which, in turn, can lead to a significant reduction in material cost.

The application of the slip PMC in this paper is for a wind energy conversion system. The slip PMC is to be interfaced with a direct-grid-connected PMSG topology, which is known as the SS PMG, as has been only very recently proposed in [8]. The slip PMC provides the damping necessary in order to allow the direct grid connection of the synchronous generator. In this paper, the main focus is to investigate the feasibility of replacing the conventional eddy-current couplings with the topology in Fig. 1(d). Several different toothed slip PMCs are evaluated and optimally designed by means of finite element (FE) methods, to the specifications of a 15-kW SS-PMG wind turbine system. Although the final design requirements will be different, the design methodology can be also applied to the design of slip-PMC devices for overall use in the industry. With a clear design criterion lacking for the slip PMC, this aspect is addressed in this paper by determining the most important performance constraints and to achieve the optimum design by evaluating several different slip-PMC concepts on the basis of active mass, PM content, and manufacturability.

III. Case Study: SS PMG

Although direct-grid-connected synchronous generators are not commonly used in the wind industry, there are certain advantages with regard to this topology, such as increased reliability due to no power electronic converter being used (the power electronic converter is one of the components considered the most unreliable in reliability analysis of wind turbine systems [9], [10]) and an increase in grid inertia and a much higher reactive power supporting capability. Examples of proposed topologies in literature where damping devices, hydraulics, and variable-speed gearboxes are utilized in conjunction with a synchronous generator are reported in [11]–[14]. The direct-grid-connected 15-kW SS PMG considered as a case study in this paper is based upon a PM induction generator (PMIG), which stems from the proposal in 1926 by [15]. It was proposed for use in a geared wind turbine system for the first time by [16] and later on for direct-drive systems by [17] and [18].

The SS PMG, as shown in Fig. 2(a), with the equivalent circuit shown in Fig. 2(b), consists of two integrated PM machine units. It differs from the conventional PMIG system due to the fact that the two machine units are magnetically separated. The only linkage between the two units is the mechanical link through the common PM rotor. The one-generator unit is a normal PMSG with its stationary stator connected to the grid.

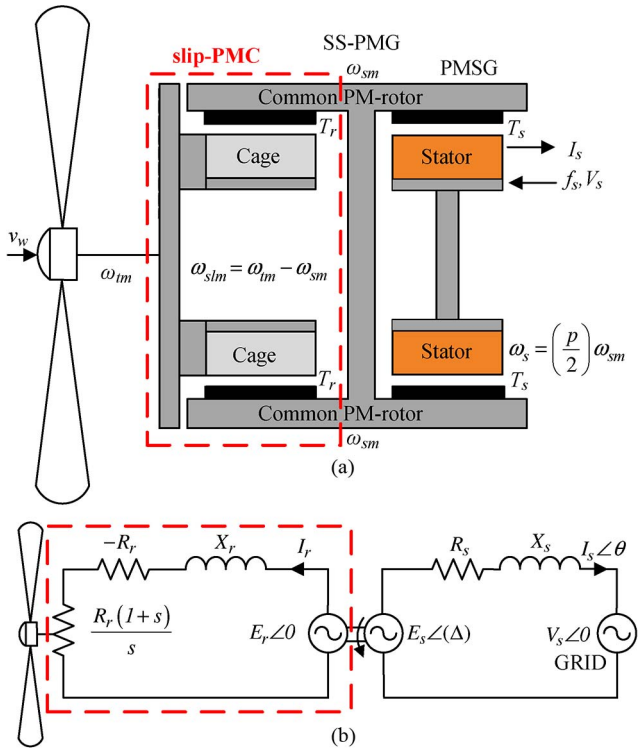

Fig. 2. (a) Cross-section diagram and (b) equivalent circuit of the new concept SS PMG [8].

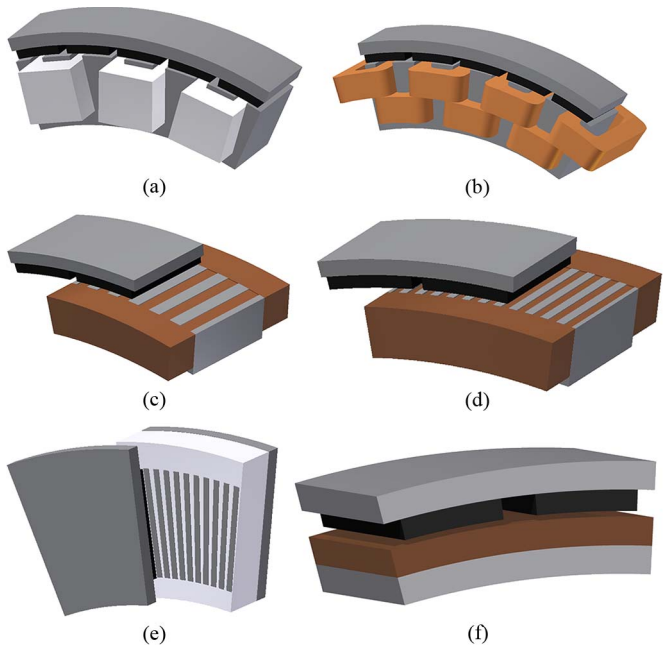

Fig. 3. (a) SL nonoverlap, (b) DL nonoverlap, (c) conventional overlap, (d) radial-flux brushless dc, and (e) axial-flux brushless dc slip-PMC configurations. (f) Conventional eddy-current coupling [7].

The other unit is the slip-PMC proposal of this study, which allows for smooth transfer of the transient turbine torque to the common PM rotor. The short-circuited slip rotor of the slip PMC runs at slip speed with respect to the synchronously rotating PM rotor. It is also possible to implement the SS PMG in conjunction with a gearbox, as a medium- or a high-speed generator, which means that the per-unit mass increase for the generator is not as severe as for direct-drive systems. The use of a wound synchronous generator instead of the PMSG, which is shown to be feasible by some due to the high price of PM materials, is also possible. Further aspects with regard to the advantages and disadvantages of the SS-PMG system are discussed in [8] and [19].

IV. Different Slip-PMC Technologies

Due to the slip PMC only transferring torque, a large amount of freedom exists in the design, which means that several different topologies can be considered. Fig. 3(a) and (b) shows a nonoverlap winding single-layer (SL) topology and a double-layer (DL) topology, respectively. The DL winding is shown in [8] and [20] to perform better than the SL winding, but the DL slip PMC is more difficult to manufacture if solid windings are used. In this paper, the SL winding is again considered due to its simple construction. However, for the DL winding, a slight modification is made. Instead of connecting the two adjacent nonoverlap coils in series, each coil is short-circuited individually, which means that solid bar windings can be used without difficulty for the DL winding as well.

To improve the torque performance of the slip PMC, a conventional three-phase overlap cage winding, as shown in Fig. 3(c), is investigated. Overlap windings, however, are known to have a large torque ripple. An interesting observation was made with the evaluation of overlap cage winding slip PMCs that if the number of slots per pole is increased, the torque ripple decreases accordingly. Observed also was that the current induced in each bar mimics the working of a brushless dc machine, as shown and explained later in this paper. An example of such a machine structure is shown in Fig. 3(d).

The slot size of the brushless dc slip PMC, as shown in the structure in Fig. 3(d), grows extremely small due to the large amount of slots. The smaller the slot size becomes, the more difficult it becomes to manufacture the machine, due to the problem of adequately fixing the bars to the end rings. The bar/end ring connection is extremely important, and if the contact resistance becomes too large, the torque performance and efficiency of the machine are significantly reduced. For this reason, the brushless dc concept is also proposed as an axial flux machine, as shown in Fig. 3(e). For an axial flux slip PMC, the cage can be easily manufactured as one solid piece. The solid cage can be then fixed to a solid steel disk, which acts as the slip-rotor yoke. In this case, there is no contact resistance in the electrical circuit. The manufacturing of the brushless dc slip PMC becomes more feasible in this case, and it is also possible to utilize a large part of the construction mass as part of the active mass in a typical wind generator topology as for this specific application. However, in this case, single-rotor axial flux PM machines are known to have exceptionally large attraction forces between the PM rotor and the slip rotor.

In [7], an eddy-current coupling similar to the topologies in literature is proposed for use in the SS-PMG setup. Although the modeling of this machine is not dealt with in this particular paper, the results from [7] are included for comparison purposes. In most cases, it is important that torque is transferred

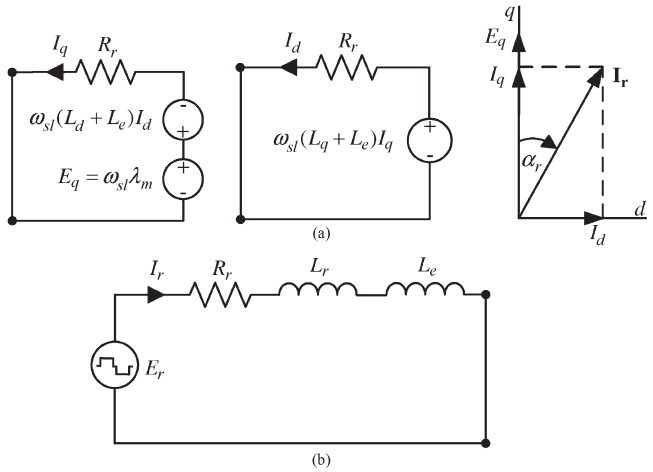

Fig. 4. (a) dq equivalent modeling and vector diagram and (b) brushless dc modeling used to calculate the bar currents of the slip PMC.

smoothly. In this regard, the conventional toothless eddy-current coupling should have an advantage due to it having zero torque ripple. Conventional type eddy-current couplings should be also easier to manufacture than the toothed proposals, as proposed in this paper. A prototype example structure is shown in Fig. 3(f). For further reduction in material costs, the viability of using aluminium instead of copper as conductor material is also considered in this paper.

V. Slip PMC Modeling

Two types of modeling are done for the slip PMCs in this study. The induced rotor bar currents of some of the slip PMCs (DL and SL nonoverlap) are sinusoidal, and these machines can be modeled in the dq reference frame. However, for the brushless dc slip PMCs, the current waveforms induced in the bars are trapezoidal or quasi-square wave in nature, as shown in Fig. 6. A flat-topped dc magnitude is observed, which corresponds to the magnet pitch σ_m. Due to this flat current profile, the bar current is considered as a dc quantity during conduction, which simplifies the modeling significantly.

A. dq Equivalent Circuit Modeling

From Fig. 4(a), the steady-state dq equations of the short-circuited slip-PMC unit, with positive current taken as flowing out and I_{dr} and I_{qr} being the dq currents, are respectively given by

$$0 = -R_r I_q - \omega_{\rm sl}(L_d + L_e)I_d + \omega_{\rm sl}\lambda_m \tag{1}$$

$$0 = -R_r I_d + \omega_{\rm sl}(L_q + L_e)I_q \tag{2}$$

where $\omega_{\rm sl}$ is the electrical slip speed equal to $\omega_{\rm sl} = \omega_t - \omega_s$, with ω_t being the electrical turbine speed and $\omega_s = 2\pi f_s$ the electrical speed of the common PM rotor. The dq inductances in (1) and (2) and Fig. 4(a), with λ_d, λ_q, and λ_m indicating the dq and PM flux linkages, respectively, are defined as

$$L_q = \frac{\lambda_q}{-I_q} \quad L_d = \frac{\lambda_d - \lambda_m}{-I_d}. \tag{3}$$

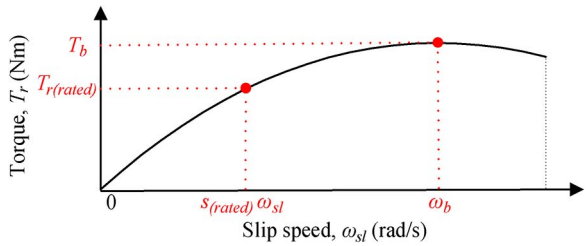

Fig. 5. Typical torque versus slip curve of the slip PMC.

The per-phase end-winding inductance is indicated by L_e in (1) and (2) and Fig. 4 and can be calculated either by analytical methods or FE analysis, as discussed in [21]. The general relations of current and copper losses are given by

$$\begin{bmatrix} I_q \\ I_d \end{bmatrix} = \sqrt{2} I_r \begin{bmatrix} \cos\alpha_r \\ \sin\alpha_r \end{bmatrix} \tag{4}$$

$$I_q^2 + I_d^2 = 2I_r^2 \tag{5}$$

$$I_r^2 = \frac{P_{\rm cu}}{3R_r} \tag{6}$$

with $P_{\rm cu}$ being the copper loss, R_r the per-phase bar resistance, and α_r the current angle. The developed torque of the slip PMC is expressed as

$$T_r = \frac{3}{4} p\left[(L_q - L_d)I_d I_q + \lambda_m I_q\right]. \tag{7}$$

The efficiency is given by

$$\eta_r = \frac{P_r}{P_t} = \frac{T_r \omega_{sm}}{T_r \omega_{tm}} = 100 \times (1 - s) \tag{8}$$

where the subscript "m" in (8) denotes the mechanical speed; and P_t and P_r indicate the mechanical turbine input and the output power of the slip PMC, respectively.

Another very important parameter in the design of the slip PMC is the breakdown torque T_b. Fig. 5 shows a typical slip-PMC torque versus slip curve, which clearly shows the operating torque and breakdown torque regions. However, calculating this parameter accurately is difficult. To get an indication of the value of this parameter, $\omega_{\rm sl}$ needs to be calculated where the derivative of (7) with respect to $\omega_{\rm sl}$ is equal to zero. The first step is to rewrite (1) and (2) in order to have I_d and I_q in terms of $\omega_{\rm sl}$. This gives the following for I_d and I_q, respectively:

$$I_d = \frac{\omega_{\rm sl}^2 \lambda_m (L_q + L_e)}{R_r^2 + \omega_{\rm sl}^2 (L_d + L_e)(L_q + L_e)} \tag{9}$$

$$I_q = \frac{\omega_{\rm sl} \lambda_m R_r}{R_r^2 + \omega_{\rm sl}^2 (L_d + L_e)(L_q + L_e)}. \tag{10}$$

By substituting (9) and (10) into (7), the following expression for T_r in terms of $\omega_{\rm sl}$ is obtained:

$$T_r = \frac{3}{4} p \lambda_m^2 R_r \left[\frac{\omega_{\rm sl}^3 (L_q - L_d)(L_q + L_e)}{\left(R_r^2 + \omega_{\rm sl}^2 (L_d + L_e)(L_q + L_e)\right)^2}\right] + \frac{3}{4} p \lambda_m^2 R_r \left[\frac{\omega_{\rm sl}}{\left(R_r^2 + \omega_{\rm sl}^2 (L_d + L_e)(L_q + L_e)\right)}\right]. \tag{11}$$

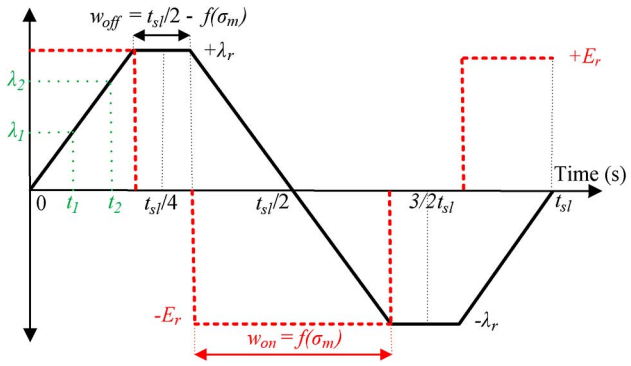

Fig. 6. Typical flux linkage and voltage waveform for the brushless dc slip PMC.

However, finding the derivative of (11) is a complex mathematical exercise. Observing (7) and knowing that $L_d \approx L_q$ for the machines considered, it can be concluded that the maximum torque is dominated by the term $\lambda_m I_q$. It would be much easier to find $\omega_{\rm sl}$ where I_q is at a maximum. With I_q as given in (10), i.e.,

$$0 = \frac{dI_q}{d\omega_{\rm sl}} = R_r^2 - \omega_{\rm sl}^2(L_d + L_e)(L_q + L_e) \tag{12}$$

and, finally,

$$\omega_b \approx \frac{R_r}{\sqrt{(L_d + L_e)(L_q + L_e)}}. \tag{13}$$

The value for the breakdown slip speed ω_b calculated in (13) can be now used in (11) to calculate T_b. It is also shown in the results section of this paper that, for the machines considered, the torque curve has a very flat profile in the region of the breakdown torque. The calculated value of ω_b in (13) should be thus sufficient as slight variations in $\omega_{\rm sl}$ will not influence the torque result significantly in the region of the breakdown torque.

B. Brushless DC Modeling

For the brushless dc machine, with the voltage waveform known to be quasi-square wave in nature, as shown in Fig. 6, the flux linkage waveform will be more or less triangular, as also shown in Fig. 6. Thus, if the gradient of the flux linkage waveform, i.e., $\lambda_{r(t)}$, is known, the bar voltage E_r can be calculated as

$$E_r = \frac{d\lambda_r(t)}{dt} = \frac{\Delta\lambda}{\Delta t}. \tag{14}$$

If the peak flux linkage λ_r is known (in this paper, it is calculated by means of FE analysis) and knowing that the peak value occurs within one quarter period of the flux linkage waveform with $\Delta t = 1/4t_{\rm sl}$, $E_{r(\rm bar)}$ can be calculated as

$$E_r = \frac{p}{\pi}\lambda_r\omega_{\rm slm} = K_r\omega_{\rm slm}, \qquad \omega_{\rm slm} = \frac{4\pi}{p}f_{\rm sl} \tag{15}$$

with the armature reaction ignored. The subscript m denotes the mechanical speed in this case, $f_{\rm sl}$ is the electrical slip frequency, and K_r is the machine constant.

From the equivalent circuit for the brushless dc slip PMC, as shown in Fig. 4(b), the induced current, i.e., $I_{r(\rm bar)DC}$, of the machine can be calculated as

$$I_{r(\rm bar)DC} = \frac{E_r}{R_{r(\rm bar)}} \tag{16}$$

with the bar resistance $R_{r(\rm bar)}$ analytically calculated from the given slot and end-ring dimensions. With $I_{r(\rm bar)DC}$ known, the developed torque of the brushless dc slip PMC can be calculated for low slip values as

$$T_r = mK_rI_{r(\rm bar)DC}, \qquad m = S \times \sigma_m. \tag{17}$$

The variable m in (17) indicates the effective number of bars active at any given time instance and is given as a function of the magnet pitch σ_m and the total number of slots S of the slip rotor.

Due to the current waveform of the brushless dc slip PMC becoming more sinusoidal in nature for higher slip values, T_b is approximated with a per-phase equivalent approach, where S/p effectively indicates the number of phases. Thus, for higher slip values, with only the fundamental of the current and voltage waveforms considered, the torque is given by

$$T_r = \frac{I_r^2R_r}{\frac{2}{p}\omega_{\rm sl}} \times \frac{S}{p} = \frac{2SI_r^2R_r}{\omega_{\rm sl}} \tag{18}$$

and with the voltage per bar the same as the voltage per phase and given by (15), the RMS current can be written as

$$I_r = \frac{pK_r\omega_{\rm sl}}{\sqrt{2\left(R_r^2 + (L_r\omega_{\rm sl})^2\right)}}. \tag{19}$$

By substituting (19) into (18), the torque is given as

$$T_r = p^2K_r^2R_rS\frac{\omega_{\rm sl}}{R_r^2 + (L_r\omega_{\rm sl})^2}. \tag{20}$$

To obtain the maximum torque, $\omega_{\rm sl}$ needs to be calculated where the derivative of (20) is equal to zero. Thus, with

$$0 = \frac{dT_r}{d\omega_{\rm sl}} = R_r^2 - (L_r\omega_{\rm sl})^2 \tag{21}$$

the slip speed where the maximum torque occurs, i.e., ω_b, is given as

$$\omega_b \approx \frac{R_r}{L_r}. \tag{22}$$

By substituting (22) into (20), the breakdown torque T_b can be finally approximated as

$$T_b \approx \frac{K_r^2p^2S}{2L_r} \tag{23}$$

with L_r being the inductance per phase.

C. FE Simulation Procedure

Due to the large number of optimizations required for this study, it is beneficial that the solving time be reduced. Instead of using transient FE analysis that takes time, a number of

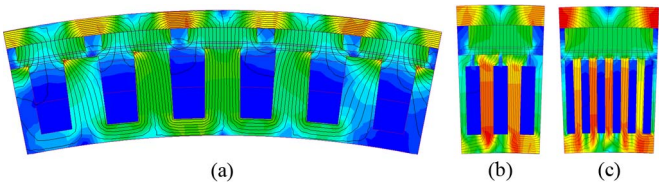

Fig. 7. FE models and field plots with (a) DL nonoverlap, (b) overlap, and (c) brushless dc slip-PMC winding configurations.

nonlinear static FE solutions are used in combination with the equations given above to obtain the operating state of the slip PMC and the performance of the machine at this operating point. The performance is calculated at a specified slip point in all cases. For both the machine types analyzed, i.e., with dq and brushless dc analysis, respectively, a minimum of three static FE solutions is required to simulate the performance of the machine at the specific slip operating point. Fig. 7(a)–(c) shows the FE models and field plots of three of the different slip-PMC configurations, as discussed in Section III.

1) FE Combined With dq Modeling: For the slip PMCs analyzed by means of dq equivalent analysis, the same FE modeling procedure thoroughly explained in [8] is used. A minimum of three static FE simulations is required to obtain the operating point and the performance of the machine at this point. The abc flux linkages λ_{abc} are obtained at each static FE iteration. These flux linkages are transformed to the dq reference frame and are then used to solve (1)–(13) to obtain the operating point and performance of the machine.

2) FE Combined With Brushless DC Modeling: To solve (15)–(23) for the brushless dc machines, the magnitude of the machine constant K_r is required to calculate the machine performance parameters. It is known from (14) that E_r can be calculated from the derivative of the flux linkage waveform, as shown in Fig. 6. Although the waveform is triangular in nature, a flat-topped quantity is observed, corresponding to σ_m, which leads to a dead band in the voltage waveform. Thus, with two static FE simulations, it is possible to calculate two points, i.e., (t_1, λ_{r1}) and (t_2, λ_{r2}), in the linear region of the $\lambda_r(t)$ waveform, as shown in Fig. 6. E_r can be now calculated from (14), with $\Delta\lambda = \lambda_{r2} - \lambda_{r1}$ and $\Delta t = t_2 - t_1$. With E_r known, K_r can be calculated from (15), and finally, (16) and (17) can be solved.

To calculate the breakdown torque of the brushless dc machine, the total per-phase inductance L_r is required. This value is calculated by exciting m number of cage-rotor bars with rated current as calculated in (16) to take the mutual phase cross coupling into account. The inductance can be then calculated as

$$L_r = \frac{\lambda_r}{I_r} + L_e \tag{24}$$

where λ_r is the flux linkage per bar, and L_e is again calculated by means of the methods discussed in [21]. With L_r known, (22) and (23) can be solved for ω_b and T_b.

VI. Design Optimization

The design optimization is done by means of the *Visual Doc* optimization suite [22]. As in [8], the optimization algorithm is coupled with static FE modeling methods as discussed above in Section IV. It is also important that the design criteria of the slip PMC are correctly set up for the particular application.

TABLE I
Design Constraints of the Slip PMC

Parameter	Value
Rated torque ($T_{r(rated)}$), Nm	1000
Rated slip ($s_{(rated)}$), pu	0.03
Breakdown torque (T_b), pu	≥ 2.0
No load torque ripple ($\Delta\tau_{NL}$), %	≤ 2.0
Full load torque ripple ($\Delta\tau_L$), %	≤ 4.0
Synchronous speed (n_s), r.min^{-1}	150
Electrical output power (P_s), kW	15
Maximum outer diameter (D_o), mm	655
Maximum axial stack length (l), mm	≤ 150

A. Optimization Constraints and Methodology

As mentioned, the slip PMC in this study needs to be implemented in an SS-PMG wind turbine system. The optimum design of the PMSG unit is discussed in [23]. With the SS PMG consisting of two integrated electrical generators, an important aspect is the extra mass and the PM material added to the design, as well as the added complexity of the SS-PMG generating system as opposed to other electrical wind generators. The importance of reducing the mass and the PM content of the slip PMC unit while still keeping the system mechanically as simple as possible is clear. Thus, all of the machine structures discussed in Section III are optimized subject to certain design constraints from the specific 15-kW SS-PMG wind turbine system for minimum active and PM mass.

The physical design constraints are given in Table I. The rated torque, i.e., $T_{r(\text{rated})}$, corresponds to the torque value on the turbine curve at the rated power and speed as given in Table I. With efficiency deemed important in this case, for each of the optimized slip PMCs, the specified rated slip of $s_{(\text{rated})} = 0.03$ p.u. corresponds to the efficiency from (8) of 97%. With the efficiency of the PMSG unit given in [23] as 94%, the total system efficiency is just over 91%, which compares well with other wind turbine drive train topologies currently in use. As explained in [19], the slip PMC can achieve much higher efficiencies, much more easily compared with the PMSG unit. In order to allow for stable operation of the direct-grid-connected SS PMG, previous practical iterations and dynamic studies seem to indicate a no-load cogging torque $\Delta\tau_{\text{NL}}$ of not more than 2% and a load torque ripple $\Delta\tau_{\text{L}}$ of not more than 4% [24]. In [19], it is mentioned that, due to the low frequency of the torque ripple of the slip PMC, it can be transferred to the grid under certain conditions. Shown in Fig. 21 is the bandwidth of the distortion of the stator torque response $\Delta\tau_s$ due to the torque ripple disturbance of the slip PMC, i.e., $\Delta\tau_r$. This same distortion will be thus seen in the stator current injected into the grid, which could cause unwanted flickering effects. Furthermore, from the specifications of the case study 15-kW wind turbine system, the maximum allowable outer diameter of the generator is fixed at $D_o = 655$ mm. To prevent the generator overhang from becoming too long, it is

TABLE II
OPTIMIZATION RESULTS AND COMPARISON OF THE CONVENTIONAL EDDY-CURRENT COUPLING AND THE SL AND DL NONOVERLAP SLIP PMCS

	Eddy-current [7]	Non overlap-SL		Non overlap-DL	
	Cu	Al	Cu	Al	Cu
T_b, pu	8.00	2.00	2.02	2.01	2.11
$\Delta\tau_{NL}$, %	0.00	2.54	1.43	1.65	1.94
$\Delta\tau_L$, %	0.00	3.12	3.91	1.18	1.82
l, mm	123.8	131.8	124.7	107.1	90.50
D_i, mm	564.5	579.0	593.0	562.0	578.0
M_{PM}, kg	24.0	5.57	5.08	5.62	4.48
M_{cond}, kg	14.0	12.2	21.5	12.5	23.2
M_{Fe}, kg	27.3	43.0	34.5	38.3	33.1
M_{Tot}, kg	65.3	60.7	61.1	56.3	60.8

Eddy-current coupling: Very simple construction. Zero torque ripple. Better susceptibility to misalignment. High mass and very high PM content.

SL non overlap: Simple construction. Easy use of aluminium. No contact resistance. High mass and PM content. Long stack length.

DL non overlap: Easy construction. Easy use of aluminium. No contact resistance. High mass and PM content, but lower than SL.

TABLE III
OPTIMIZATION RESULTS OF THE THREE-PHASE OVERLAP AND BRUSHLESS DC SLIP PMCS

	Overlap 3-phase		Brushless-DC radial Flux		Brushless-DC axial Flux	
	Al	Cu	Al	Cu	Al	Cu
T_b, pu	2.02	2.02	2.03	2.40	2.10	2.39
$\Delta\tau_{NL}$, %	5.56	3.76	1.64	1.97	1.33	0.93
$\Delta\tau_L$, %	10.78	9.94	0.44	0.71	2.28	2.61
l, mm	82.0	66.5	62.5	55.0	55.5	44.6
D_i, mm	565.0	577.0	570.0	580.6	490.0	533.2
M_{PM}, kg	3.53	3.43	3.53	3.51	3.62	3.49
M_{cond}, kg	8.99	17.05	7.22	12.38	10.16	16.34
M_{Fe}, kg	28.18	20.14	22.25	15.98	14.97	6.97
M_{Tot}, kg	40.70	40.62	33.0	31.87	28.76	26.80

Overlap 3-phase Moderate to difficult construction. Depending on machine size aluminium casting is possible. Contact resistance is a problem if not cast. Medium to low mass and low PM content. High torque ripple.

Brushless-DC-radial Very difficult construction. Aluminium use might be difficult. Contact resistance is a problem. Low mass and PM content. Low torque ripple.

Brushless-DC-axial Moderate to easy construction. Easy use of aluminium. No contact resistance. Low torque ripple. Very low mass and PM content. Large attraction forces.

suggested that the axial length of the slip PMC should be at least less than 150 mm, preferably as short as possible.

Important also to consider is the demagnetization of the PMs, due to the fact that the slip PMC is basically a short-circuited PM generator. Care needs to be taken because of the possible high short-circuit currents. In addition, due to some of the components such as the PMs and steel yokes of the slip PMC being solid for easier manufacturing, the temperature can rapidly increase due to eddy-current losses if the slip PMC over speeds. With a rise in temperature, demagnetization of the PMs becomes even more of a concern. The operating temperature, thus, also needs to be considered as is important in many eddy-current coupling applications.

B. Optimization Results

Table II gives the optimization results for the SL and DL nonoverlap slip PMCs, Table III gives the optimization results for the three-phase overlap and radial and axial flux brushless dc slip PMCs, and Fig. 8 shows a summary of the different active mass components of all the slip PMCs. In order to compare these results with those of conventional eddy-current couplings, the optimization results obtained in [7] for the same design specifications as in this paper are also given in Table II. The two dimensions given are the axial stack length l and the inside diameter D_i of the machine. The mass quantities shown are the PM mass $M_{\rm PM}$, the conductor mass M_C, the steel mass $M_{\rm Fe}$, and the total active mass $M_{\rm Tot}$. The different slip-PMC configurations are also evaluated with regard to complexity and ease of manufacturing.

For the results shown in Table III, the optimization is done subject to a constraint on the maximum allowable value of $M_{\rm PM}$ at about 3.5 kg. For the nonoverlap winding machines, the value of $M_{\rm PM}$ shown is for the minimum achievable value of PM mass, whereas the design still complies with the limits set in Section V-A. The relationship between $M_{\rm Tot}$ and $M_{\rm PM}$ is shown in Fig. 9. In Fig. 9, the upper allowed limit for the PM mass is gradually reduced until the design no longer complies with the limits set in Section V-A. For all the design cases, except for the conventional eddy-current coupling, the machines are optimized for both copper and aluminium used as conductor. In [7], aluminium was not considered as a conductor as the amount of PM material required for the specific application becomes too high.

From Tables II and III and Fig. 8, it is clear that the brushless dc slip-PMC configurations yield much lower active mass and lower PM content due to the much better torque performance of these winding types. This is particularly true for the axial flux machine where, for this particular application, certain parts of the construction mass and the active mass can be combined as mentioned. It is also clearly shown that the slip-PMC topologies evaluated in this paper use a considerably lower amount of PM material as opposed to conventional eddy-current couplings. Depending on the topology used, the active mass can be also substantially reduced. Furthermore, surprisingly, it is shown that, by using aluminium instead of copper as conductor material, the performance with regard to active mass and PM content is not that much different. The aluminium machines also have a much lower value for M_C, and it should be noted that aluminium is significantly cheaper than copper. It is true that the aluminium machines have a higher value for $M_{\rm Fe}$, but steel is even cheaper than aluminium. Thus, for the same PM mass, the aluminium machines are much cheaper per unit mass than the copper machines. An advantage of the copper machines, however, is that a slightly lower PM mass can be specified, as shown in Fig. 9. The copper machines yield a lower minimum PM mass due to the fact that the aluminium machines have a larger steel volume, which increases the per-phase inductance, which, in turn, influences the value for the maximum torque, as shown in (11) and (23).

As mentioned, in this study, the slip PMC forms part of a small-scale wind turbine system. For the 15-kW SS-PMG wind turbine system, the total tower top mass without the slip PMC is about 500 kg. A construction mass of about 40 kg needs to be added for all the slip-PMC topologies as only the active mass is shown. The total system mass can be estimated

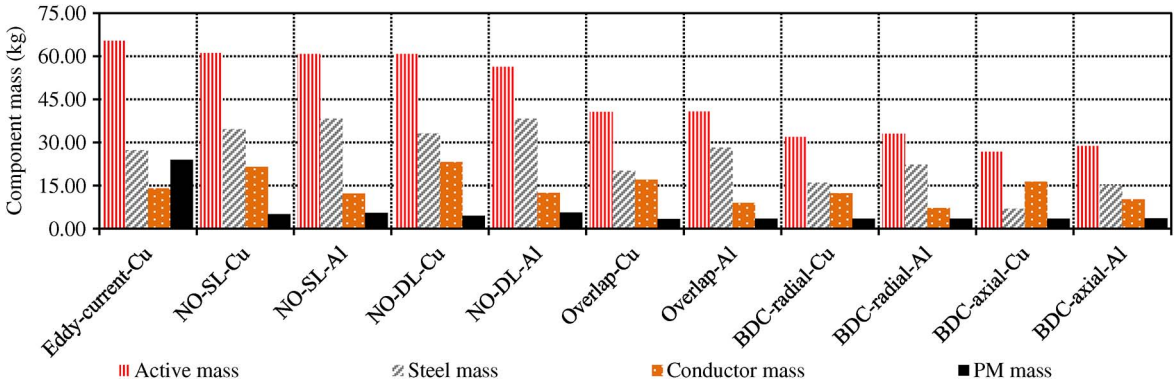

Fig. 8. Comparison of total active, steel, conductor, and PM mass components of the different optimum slip-PMC configurations.

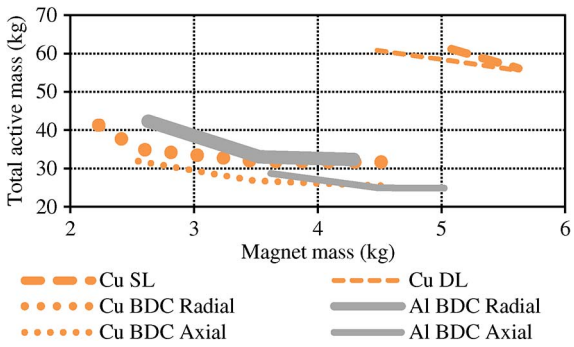

Fig. 9. Active mass versus PM mass for the SL and DL nonoverlap and brushless dc (BDC) radial flux and axial flux slip PMCs.

as $M_{\mathrm{System}} = 540 + M_{\mathrm{Tot}}$ kg, where M_{Tot} is the optimized active mass for each topology shown in Tables II and III. Thus, depending on the topology used, the per-unit increase in total system mass by adding the slip PMC to the system varies between 1.12 and 1.2 p.u.

VII. Prototype Machine Evaluation

For the practical evaluation, five prototype slip-PMC configurations are considered. The simulation results for these five machines are presented as these are the only slip-PMC configurations that were manufactured and practically evaluated.

A. Prototype Slip PMCs

It should be noted that the machines shown in Fig. 10(a)–(f) are not all optimally designed as in Tables II and III. The machines here are merely used to validate the operating principles of the various technologies and to verify the FE results. The SL machine shown in Fig. 10(a) with solid bar coils is a very simple unoptimized structure, which fits within the dimensions of the DL machine in Fig. 10(b). In previous studies such as in [20], the DL slip PMC made use of a wound slip rotor due to the difficulty of connecting the two adjacent solid bar coils in series. However, as shown in [20], it is possible to short-circuit each coil individually, which means that solid bar coils can be used for the DL nonoverlap slip PMC, as shown in Fig. 10(b), and, in a similar way, for the SL nonoverlap winding slip PMC.

Fig. 10(c) shows the overlap winding slip PMC, which is similar to squirrel-cage induction machine rotors commonly used in the industry. In this case, the cage winding is cast with aluminium, similar to the processes commonly employed in the industry. However, as shown in the results in Table III, the overlap winding has a problem with torque ripple. To reduce the torque ripple, a very simple skewing concept for the PMs is employed. Due to the high pole number and the relatively large diameter used, it is possible to make the PM flat instead of curved. This makes manufacturing much easier, and a solid flat skewed magnet is the result, as shown in Fig. 11(a). The PM rotor laminations also need to be adapted in order to accommodate the flat profile of the PMs. Fig. 10(d) shows a conventional eddy-current coupling, as evaluated in [7]. This machine structure corresponds to the eddy-current coupling topology shown in Figs. 1(c) and 3(f). A copper ring is pressed

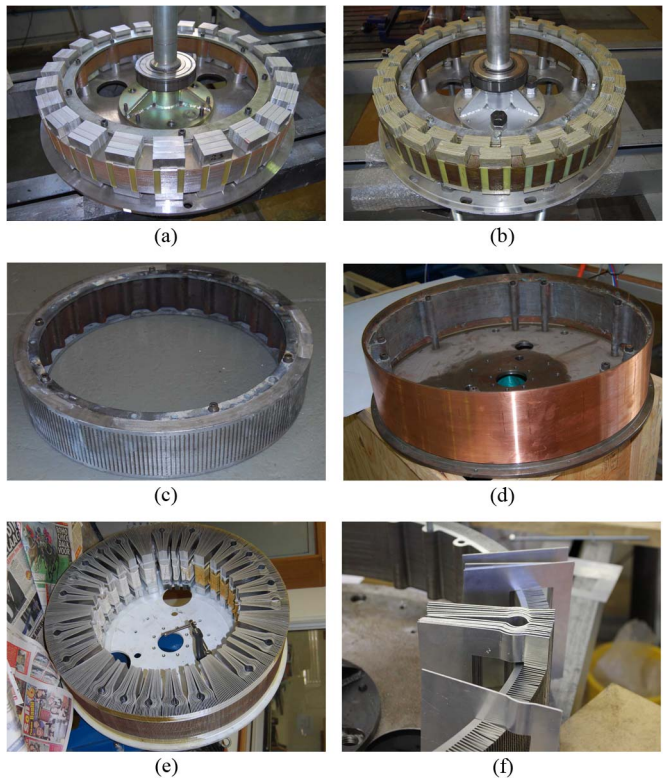

Fig. 10. (a) SL nonoverlap, (b) DL nonoverlap, (c) cast overlap cage winding, (d) conventional-type eddy-current coupling [7], and (e) brushless dc slip-PMC prototype slip rotors, with (d) displaying how the thin solid bar coils are being shifted into position for the brushless dc slip PMC.

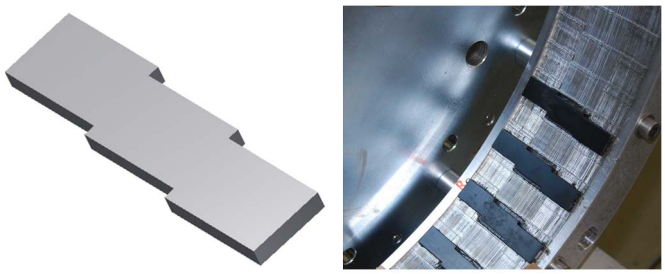

Fig. 11. (a) Solid flat skewed magnet concept utilized for the overlap winding slip PMC. (b) Skewed PMs, being fixed to the slip-PMC side of the common PM rotor.

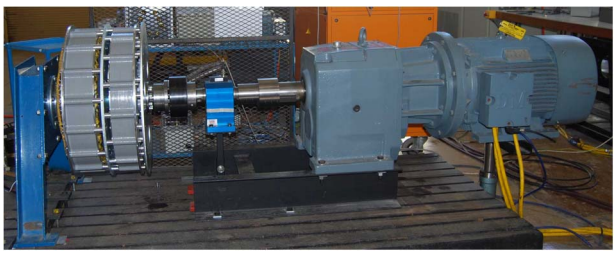

Fig. 12. SS-PMG system of 15 kW on the test bench connected to a driving motor on the right through a torque sensor shown in the middle.

over a laminated steel yoke, with the machine designed to fit within the dimensions of the PM rotor of the brushless dc slip PMC in Fig. 10(e).

Due to the difficulty of fixing the very thin bars of the brushless dc slip PMC to the end rings and the problem of contact resistance, a different approach is followed for the manufacturing of this machine. In this case, each bar is an individually short-circuited coil with the current return path underneath the stack, as shown in Fig. 10(f). These solid bar coils are cut from very thin sheets of aluminium. The coils are shifted into position through a central opening in the lamination stack, which is filled up after all the other coils are in position. Although this is not an optimum solution due to the very long current return path and, thus, high resistance, this prototype is sufficient to validate the concept of a brushless dc slip PMC. Fig. 12 shows the SS-PMG system with the slip PMC mounted at the front of the SS PMG being laboratory tested. An induction machine controlled by means of a variable-frequency drive is used as a prime mover.

B. Steady-State Results

Fig. 13 shows the torque versus slip profiles of the different manufactured slip-PMC prototypes. It is shown that the DL nonoverlap winding machine has a higher breakdown torque value than the SL winding slip PMC in this case. The brushless dc machine, on the other hand, has more than double the maximum torque of the DL winding slip PMC. What is interesting is that, in this case, all three slip PMCs have more or less similar mass and PM content. The torque versus slip profile of the eddy-current coupling from [7] is also shown in Fig. 13. The curve shown was calculated by means of 3-D FE analysis, with the FE-predicted results practically verified in [7]. For

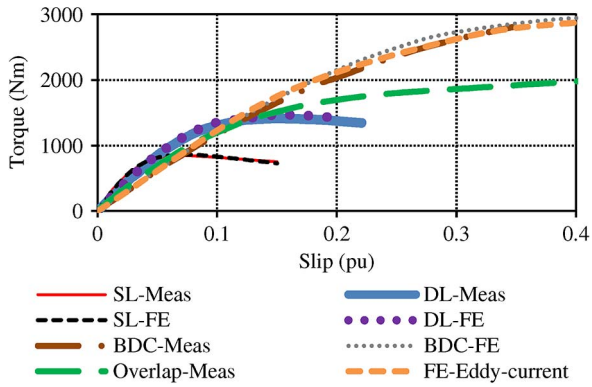

Fig. 13. Measured and FE-calculated torque versus slip of the prototype nonoverlap SL, DL, brushless dc (BDC), overlap, and conventional eddy-current coupling slip PMCs.

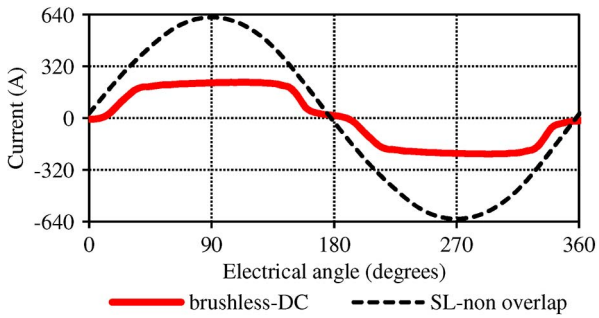

Fig. 14. FE-calculated rated bar current of the SL nonoverlap and brushless dc prototype slip PMCs versus electrical angle.

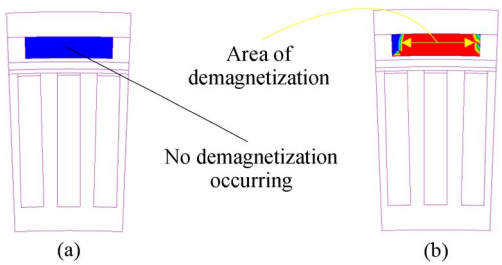

Fig. 15. FE-predicted demagnetization states of the overlap winding slip PMC at a magnet temperature of (a) 100 °C and (b) 160 °C.

the overlap cage-winding slip PMC, it should be noted that the active mass and the PM content of the prototype machine closely correspond to the optimum design for an aluminium overlap winding slip PMC in Table III. Fig. 14 shows the sinusoidally induced current per bar coil of the SL slip PMC and the quasi-square current waveform of the brushless dc slip PMC calculated by means of FE.

With demagnetization more of a concern for lower values of magnet height, i.e., h_m, such as the case for the overlap winding slip PMC with $h_m = 4.5$ mm, this phenomenon is investigated by means of FE analysis in this paper. For PMs, irreversible demagnetization effects start to occur if the PM flux density goes below the linear region of the PM BH curve, which is known as B_{demag}. In [21], typical PM BH curves are shown, as well as how these curves are influenced by PM temperature. More information on PM demagnetization theory combined with FE can be also found in [25]. In Fig. 15(a), the magnet

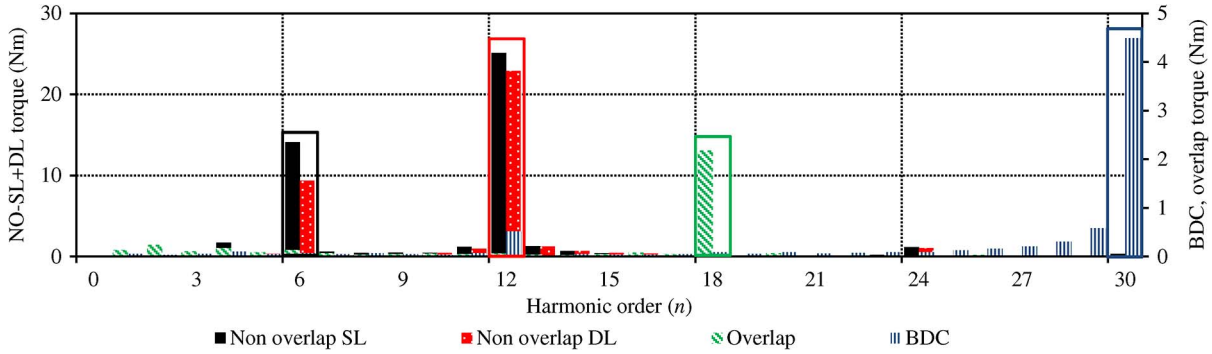

Fig. 16. Frequency spectrum of torque ripple of the SL and DL nonoverlap, brushless dc, and overlap winding slip PMCs.

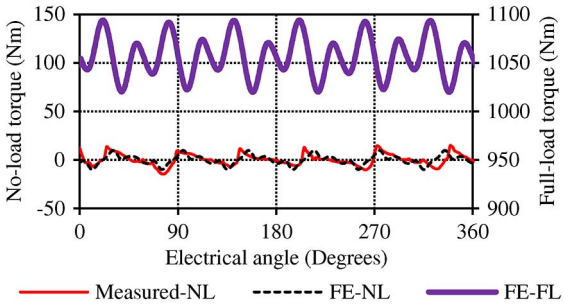

Fig. 17. FE-predicted no-load and full-load torque ripple and measured no-load torque ripple versus electrical angle of the SL nonoverlap slip PMC.

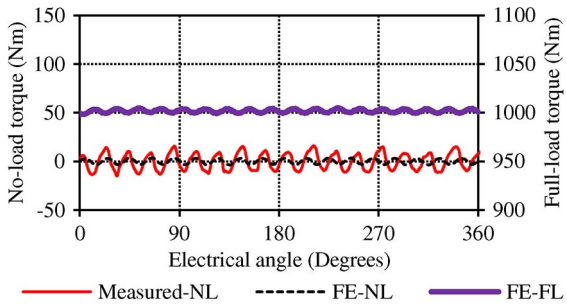

Fig. 19. FE-predicted no-load and full-load torque ripple and measured no-load torque ripple versus electrical angle of the overlap winding slip PMC.

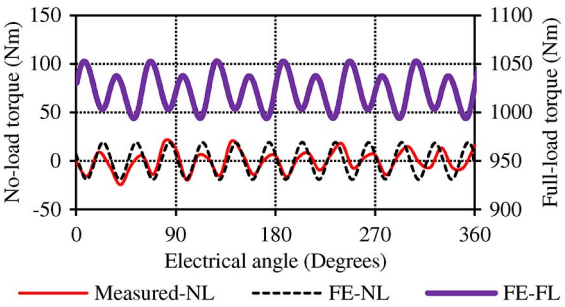

Fig. 18. FE-predicted no-load and full-load torque ripple and measured no-load torque ripple versus electrical angle of the DL nonoverlap slip PMC.

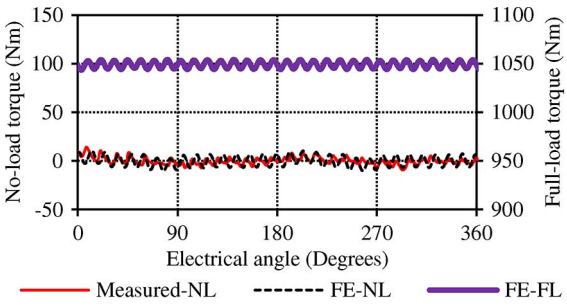

Fig. 20. FE-predicted no-load and full-load torque ripple and measured no-load torque ripple versus electrical angle of the brushless dc slip PMC.

temperature is set as 100 °C ($B_{\text{demag}} < 0$), and it is set to 160 °C ($B_{\text{demag}} = 0.7$) in Fig. 15(b). It is observed that with maximum short-circuit current flowing in the bars, only above about 100 °C do serious demagnetization effects start to occur, as indicated in Fig. 15(b) and predicted by FE analysis.

C. Torque Quality

In Figs. 17–20, the measured and FE-simulated cogging torque and the FE-predicted load torque ripple of the SL and DL nonoverlap winding, overlap winding, and brushless dc slip PMCs are shown. The no-load cogging torque is obtained by means of the static measuring method, as proposed in [26]. The brushless dc slip PMC is clearly shown to have a much lower torque ripple than the other topologies. The cogging torque measurement of the overlap winding is different from the FE prediction due to manufacturing imperfections with regard to the uniformity of the air gap. However, it is still measured at about 3%, which is close to the limits set in Section V-A. In this regard, the conventional eddy-current coupling should have an advantage as it will be able to handle misalignment better, without causing any unwanted torque ripple effects.

Furthermore, it is observed that there are clear differences between the no-load cogging torque waveforms and the load torque ripple waveforms of the different slip PMCs. There are also clear differences in the frequency content of the different torque ripple waveforms. Fig. 16 shows the frequency spectrum of the load torque ripple waveforms of the SL and DL nonoverlap winding slip PMCs and that of the brushless dc and overlap winding slip PMCs. Both the SL and DL nonoverlap winding slip PMCs have a strong harmonic component at $n = 6$ and $n = 12$. For the skewed overlap winding topology, the dominant harmonic is at $n = 18$, and for the brushless dc slip PMC, it is at $n = 30$. It should be noted that the torque ripple frequency spectrum of the overlap winding and brushless dc slip PMCs is plotted on the vertical axis to the right, due to their much smaller torque ripple amplitudes compared with the nonoverlap winding slip PMCs. Observing Fig. 21, it is shown that not only

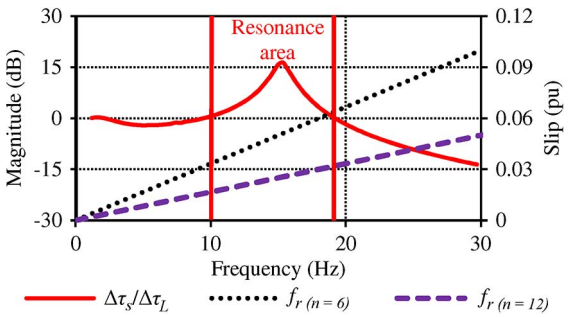

Fig. 21. Frequency response of $\Delta\tau_s/\Delta\tau_L$ of the direct-grid-connected SS-PMG system [19].

is it important to minimize the torque ripple amplitude but it is also important to evaluate the frequency spectrum of the torque ripple as certain torque ripple frequency components can fall within the resonance area in Fig. 21. It should be noted that Fig. 21 is relevant to a specific application of the slip PMC. For other industry applications, the required frequency spectrum and resonance characteristics of the slip PMC torque ripple might be different.

VIII. Conclusion

In this paper, it has been shown that the active mass (particularly the PM mass) and, thus, the material cost of a slip PMC can be substantially reduced compared with conventional eddy-current couplings. For the SS-PMG wind turbine application considered, the total increase in system mass is estimated at about 12%–20% if a slip PMC is used in addition to a same-size direct-drive PM generator.

Several new slip-PMC topologies are introduced and evaluated in this paper. For the novel brushless dc winding slip PMC, an even further reduction in active and PM mass compared with the nonoverlap winding configurations is possible. However, manufacturing, particularly with regard to the fixing of the bars to the end rings, poses a significant challenge for the brushless dc slip PMC. Other brushless dc concepts such as the axial-flux configurations are evaluated to reduce the complexity of fixing the bars to the end rings. The active mass of the axial flux machine is considerably lower due to the fact that some of the construction and active mass components of the machine can be integrated. However, the large attraction forces associated with this machine are a problem. The conventional three-phase overlap winding also shows promising results for active mass reduction, with the torque ripple problem overcome by utilizing a simple flat skewed PM topology. Furthermore, surprisingly, it is shown that aluminium can be used instead of copper without increasing the mass of the slip PMC or decreasing the machine performance. The use of aluminium has the potential to further reduce the cost of the coupling. Construction-wise, the conventional eddy-current couplings should be easier to manufacture. Alignment and air gap integrity are also less of an issue in this case, with the torque quality of these topologies much better than that of the other slip PMCs. Thus, depending on the application, these aspects need to be weighed against the reduced mass and material cost with regard to the other slip-PMC topologies.

References

[1] B. Lequesne, B. Liu, and T. W. Nehl, "Eddy-current machines with permanent magnets and solid rotors," *IEEE Trans. Ind. Appl.*, vol. 33, no. 5, pp. 1289–1294, Sep./Oct. 1997.

[2] A. Canova and B. Vusini, "Design of axial eddy-current couplers," *IEEE Trans. Ind. Appl.*, vol. 39, no. 3, pp. 725–733, May/Jun. 2003.

[3] S. E. Gay and M. Ehsani, "Parametric analysis of eddy-current brake performance by 3-D finite-element analysis," *IEEE Trans. Magn.*, vol. 42, no. 2, pp. 319–328, Feb. 2006.

[4] B. Zheng and S. Anwar, "An antilock-braking algorithm for an eddy-current-based brake-by-wire system," *IEEE Trans. Veh. Technol.*, vol. 56, no. 3, pp. 1100–1107, May 2007.

[5] N. Amati, A. Canova, F. Cavalli, and M. Padovani, "Dynamic behaviour of torsional eddy-current dampers: Sensitivity of the design parameters," *IEEE Trans. Magn.*, vol. 43, no. 7, pp. 3266–3277, Jul. 2007.

[6] L. Ye, D. Li, Y. Ma, and B. Jiao, "Design and performance of a water-cooled permanent magnet retarder for heavy vehicles," *IEEE Trans. Magn.*, vol. 26, no. 3, pp. 953–958, Sep. 2011.

[7] Z. Mouton and M. J. Kamper, "Modelling and optimal design of an eddy current coupling for slip-synchronous permanent magnet wind generators," *IEEE Trans. Ind. Electron.*, vol. 61, no. 7, pp. 3367–3376, Jul. 2014.

[8] J. H. J. Potgieter and M. J. Kamper, "Design of new concept gearless direct-grid connected slip-synchronous permanent magnet wind generator," *IEEE Trans. Ind. Appl.*, vol. 48, no. 3, pp. 913–922, May/Jun. 2012.

[9] M. Arifujjaman, M. T. Iqbal, and J. E. Quaicoe, "Reliability analysis of grid connected small wind turbine power electronics," *J. Appl. Energy*, vol. 86, no. 9, pp. 1617–1623, Sep. 2009.

[10] M. Wilkinson and G. Hendriks, "Report on wind turbine reliability profiles," Reliawind, Tech. Rep. deliverable D.1.3, 2011.

[11] A. J. G. Westlake, J. R. Bumby, and E. Spooner, "Damping the power-angle oscillations of a permanent-magnet synchronous generator with particular reference to wind turbine applications," *IEE Proc.—Elect. Power Appl.*, vol. 143, no. 3, pp. 269–280, May 1996.

[12] H. Müller, M. Pöller, A. Basteck, M. Tilshcher, and J. Pfister, "Grid compatibility of variable speed wind turbines with directly coupled synchronous generator and hydro-dynamically controlled gearbox," in *Proc. 6th Int. Workshop Largescale Integr. Wind Power Transmiss. Netw. Offshore Wind Farms*, Delft, Netherlands, 2006, pp. 307–315.

[13] M. Deldar, A. Izadian, and S. Anwar, "Modeling of a hydraulic wind power transfer system utilizing a proportional valve," in *Proc. ECCE*, Denver, CO, USA, 2013, pp. 3311–3316.

[14] S. Grabic, N. Celanovic, and V. Katic, "Permanent magnet synchronous generator cascade for wind turbine application," *IEEE Trans. Power Electron.*, vol. 23, no. 3, pp. 1136–1142, May 2008.

[15] F. Punga and L. Schon, "Der neue kollektorlose Einphasenmotor der Firma Krupp," *Elektrotech. Zeitschrift*, vol. 47, no. 29, pp. 877–881, 1926.

[16] W. F. Low and N. Schofield, "Design of a permanent magnet excited induction generator," in *Proc. ICEM*, Manchester, U.K., 1992, pp. 1077–1081.

[17] B. Hagenkort, T. Hartkopf, A. Binder, and S. Jöckel, "Modelling a direct drive permanent magnet induction machine," in *Proc. ICEM*, Helsinki, Finland, 2000, pp. 1495–1499.

[18] E. Tröster, M. Sperling, and T. Hartkopf, "Finite element analysis of a permanent magnet induction machine," in *Proc. Int. SPEEDAM*, Taormina, Italy, 2006, pp. 179–184.

[19] J. H. J. Potgieter and M. J. Kamper, "Modelling and stability analysis of a direct-drive-direct-grid slip-synchronous permanent magnet wind generator," *IEEE Trans. Ind. Appl.*, vol. 50, no. 3, pp. 1738–1747, May/Jun. 2014.

[20] J. H. J. Potgieter and M. J. Kamper, "Optimum design and technology evaluation of slip permanent magnet generators for wind energy applications," in *Proc. IEEE ECCE*, Raleigh, NC, USA, 2012, pp. 2342–2349.

[21] J. H. J. Potgieter and M. J. Kamper, "Calculation methods and effects of end-winding inductance and permanent-magnet end flux on performance prediction of nonoverlap winding permanent-magnet machines," *IEEE Trans. Ind. Appl.*, vol. 50, no. 4, pp. 2458–2466, Jul./Aug. 2014.

[22] G. N. Vanderplaats, *Multidiscipline Design Optimization*. Colorado Springs, CO, USA: Vanderplaats Research & Development, Inc., 2007.

[23] J. H. J. Potgieter and M. J. Kamper, "Design specifications and optimisation of a directly grid-connected PM wind generator," in *Proc. ECCE*, Denver, CO, USA, 2013, pp. 882–889.

[24] J. Sopanen, V. Ruuskanen, J. Nerg, and J. Pyrhönen, "Dynamic torque analysis of a wind turbine drive train including a direct-driven permanent magnet generator," *IEEE Trans. Ind. Electron.*, vol. 58, no. 9, pp. 3859–3867, Sep. 2011.

[25] S. Ruoho, E. Dlala, and A. Arkkio, "Comparison of demagnetization models for finite-element analysis of permanent-magnet synchronous machines," *IEEE Trans. Magn.*, vol. 43, no. 11, pp. 3964–3968, Nov. 2007.
[26] J. H. J. Potgieter and M. J. Kamper, "Torque and voltage quality in design optimisation of low cost non-overlap single layer winding permanent magnet wind generator," *IEEE Trans. Ind. Electron.*, vol. 59, no. 5, pp. 2147–2156, May 2012.

Johannes H. J. Potgieter (S'10) received the B.Eng. degree in electrical and electronic engineering and the M.Sc. (Eng.) and Ph.D. (Eng.) degrees in electrical engineering from Stellenbosch University, Stellenbosch, South Africa, in 2008, 2011, and 2014, respectively.

He has been employed as a Post-Doctoral Research Assistant at the University of Oxford, Oxford, U.K., since May 2014. His research interests include wind power generation technologies, automotive drive train solutions, and the design and optimization of permanent-magnet and switched reluctance electrical machines.

Maarten J. Kamper (SM'08) received the M.Sc. (Eng.) and Ph.D. (Eng.) degrees from Stellenbosch University, Stellenbosch, South Africa, in 1987 and 1996, respectively.

He has been with the Academic Staff of the Department of Electrical and Electronic Engineering, Stellenbosch University, since 1989, where he is currently a Professor of electrical machines and drives. His research interests include computer-aided design and control of reluctance, permanent-magnet, and induction machine drives.

Prof. Kamper is a South African National Research Foundation-supported Scientist and a Registered Professional Engineer in South Africa.